Research Square

Preprints are preliminary reports that have not undergone peer review.
They should not be considered conclusive, used to inform clinical practice,
or referenced by the media as validated information.

Sephin1 preserves visual circuit function and retinogeniculate integrity during autoimmune inflammatory demyelination

Gabrielle M. Mey
Michigan Medicine
Maia Jin Classe
Michigan Medicine
Jenna N. Staples
Michigan Medicine
Yanan Chen
Loyola University Chicago
Sebastian Werneburg
werneburr@umich.edu
Michigan Medicine

Research Article

Keywords: Multiple sclerosis, Experimental autoimmune encephalomyelitis, Sephin1, Integrated stress response, Visual pathway, Optic nerve, Visual evoked potentials, Retinogeniculate synapses, Oligodendrocytes, Neuroprotection

Posted Date: September 21st, 2026

DOI: https://doi.org/10.21203/rs.3.rs-10590491/v1

License: This work is licensed under a Creative Commons Attribution 4.0 International License.
Read Full License

Additional Declarations: No competing interests reported.

Abstract

Background

Multiple sclerosis (MS) causes inflammatory demyelination, axonal injury, and synaptic pathology, culminating in progressive neurodegeneration. Sephin1, an integrated stress response modulator, reduces clinical severity in experimental autoimmune encephalomyelitis (EAE) and protects spinal cord oligodendrocytes, myelin, and axons. Yet EAE clinical scores primarily measure motor disability, leaving unresolved whether Sephin1 preserves function in a defined central nervous system circuit. Here, we tested whether Sephin1 protects the visual pathway, a clinically relevant and functionally accessible circuit affected in MS.

Methods

EAE was induced in C57BL/6J mice using $MOG_{35–55}$ immunization. Sephin1 or vehicle was administered prophylactically beginning 7 days post-induction through peak disease, or therapeutically beginning at clinical onset either through chronic disease or for 7 days. Visual function was assessed by recording the optomotor response, pattern-stimulated visual evoked potentials (pVEP), and pattern electroretinography (PERG). Retina, optic nerve, and lateral geniculate nucleus (LGN) pathology were assessed using immunohistochemistry and RNA *in situ* hybridization.

Results

Prophylactic Sephin1 treatment reduced EAE clinical severity and preserved visual acuity at peak disease. Sephin1 also preserved pVEP N1 amplitude, indicating protection of visually evoked cortical response magnitude, while pVEP latency, PERG responses, and retinal ganglion cell (RGC) numbers were not significantly altered at this stage. Histologically, Sephin1 protected optic nerve axons, myelin, and oligodendrocytes. Downstream, in the LGN, Sephin1 preserved retinogeniculate axons and RGC synapses. These protective effects occurred without detectable reductions in optic nerve $CD45^+$ immune cell accumulation, $CD3^+$ T-cell infiltration, astrogliosis, or inflammatory microglial responses. Sephin1-treated EAE optic nerves showed increased p-eIF2α and *Ddit3*, with cleaved caspase-3 increased relative to controls. In contrast to prophylactic-to-peak disease treatment, Sephin1 initiated at clinical onset, either through chronic disease or for 7 days only, did not preserve chronic visual acuity.

Conclusions

Sephin1 preserves function and structure in a defined visual circuit during peak inflammatory demyelination when administered prophylactically, demonstrating circuit-level neuroprotection beyond standard EAE clinical scoring. However, onset-initiated Sephin1 treatment is insufficient to prevent chronic visual dysfunction, suggesting that ISR enhancement as a monotherapy has a limited therapeutic window in EAE-associated visual pathway injury.

BACKGROUND

Multiple sclerosis (MS) is an immune-mediated inflammatory disease of the central nervous system (CNS) characterized by demyelination, axonal injury, synaptic dysfunction, culminating in progressive circuit degeneration (1–3). Current disease-modifying therapies primarily target immune activation and have substantially improved relapse control, yet they incompletely prevent neuroaxonal damage, repair failure, and long-term disability progression (4–8). This therapeutic gap has motivated increasing interest in strategies that directly protect CNS-resident cells during inflammatory demyelination (2, 3, 9–13). Linking such tissue protection to preserved function in defined CNS circuits is therefore essential for translating neuroprotective mechanisms into clinically meaningful benefits.

One endogenous pathway that enables cells to adapt to inflammatory and proteostatic stress is the integrated stress response (ISR) (14, 15). The ISR is initiated by phosphorylation of eukaryotic translation initiation factor 2 alpha (p-eIF2α), which transiently reduces global protein synthesis while allowing selective translation of stress-adaptive transcripts (14–17). In oligodendrocyte-lineage cells, ISR activation has been shown to promote survival because the suppression of global protein synthesis reduces the load of newly synthesized proteins that must be processed by the endoplasmic reticulum (11, 18, 19). Termination of the ISR is mediated in part by growth arrest and DNA-damaged protein 34 (GADD34), which recruits protein phosphatase 1 to dephosphorylate eIF2α and restore translation (17, 20). However, the effect of ISR signaling on cellular integrity is highly context- and duration-dependent: transient activation can be cytoprotective, whereas unresolved stress signaling, including induction of C/EBP homologous protein (CHOP), encoded by *Ddit3*, may contribute to cellular dysfunction or death (21–23).

Pharmacologic enhancement of the ISR has emerged as a potential strategy to protect oligodendrocytes in MS-relevant models (11, 24, 25). Sephin1, a small molecule reported to prolong ISR signaling and maintain elevated p-eIF2α levels under stress, delays clinical disease onset and protects spinal cord oligodendrocytes, myelin, and axons in experimental autoimmune encephalomyelitis (EAE) mice, a widely used preclinical model of inflammatory demyelination (24, 26, 27). In that setting, Sephin1-mediated tissue protection was accompanied by reduced spinal cord T-cell accumulation at peak disease, although peripheral immune responses were not detectably suppressed (24). Subsequent studies demonstrated that ISR enhancement can also support remyelination in inflammatory environments, including cuprizone-induced demyelination combined with CNS interferon gamma (IFN-γ) expression, and that Sephin1 can complement oligodendrocyte differentiation-promoting agents such as bazedoxifene (28, 29). More recent mechanistic work extended these findings by showing that, in IFN-γ-stressed oligodendrocyte-lineage cells, Sephin1 further suppresses protein synthesis and promotes stress granule formation, effects consistent with enhancement of the p-eIF2α/eIF2B translational-control axis (30–32). Together, these studies provide evidence that ISR enhancement can protect oligodendrocytes and promote myelin repair under inflammatory stress.

Despite these advances, the functional consequences of Sephin1-mediated tissue protection remain incompletely defined. Prior studies provided anatomical and molecular evidence of oligodendrocyte, myelin, and axon protection; however, functional assessment in Sephin1-treated EAE mice was largely limited to standard clinical scoring (24, 28, 30). In EAE induced with myelin oligodendrocyte glycoprotein peptide 35–55 (MOG_{35-55}), early clinical scores are strongly influenced by acute spinal cord inflammatory pathology, including peripheral immune cell infiltration, blood–CNS barrier disruption, inflammatory edema, demyelination, and axonal conduction failure in motor pathways (27, 33–35). Accordingly, the previously reported delay in clinical disease after prophylactic Sephin1 treatment, together with reduced spinal cord T-cell accumulation (24), supports an effect on inflammatory disease burden at peak EAE. However, clinical scores do not directly assess circuit-specific neuronal function, synaptic integrity, or electrophysiological signaling. Thus, whether Sephin1-mediated tissue protection translates into preserved functional output within a defined, clinically relevant non-motor circuit remains unknown.

The visual system provides a powerful model to address this gap because visual dysfunction is common in MS and visual pathway injury can involve retinal ganglion cell (RGC) dysfunction, optic nerve demyelination and axon damage, and degeneration of central relay structures such as the lateral geniculate nucleus (LGN) (36, 37). This pathway enables structure–function analysis across a defined circuit: RGC somata can be assessed in the retina, their myelinated axons in the optic nerve, and their central projections and retinogeniculate synapses in the LGN. It is also well-suited for functional assessment, as the optomotor response measures visually guided acuity, pattern electroretinography (PERG) assesses RGC-related function, and pattern-stimulated visual evoked potentials (pVEP) evaluate signaling through the optic nerve and central visual pathway (36, 38, 39).

Here, we used the visual system to test whether Sephin1 preserves circuit function and structural integrity during EAE. We found that prophylactic Sephin1 treatment preserved visual acuity and pVEP amplitudes, and protected axons, myelin, and synapses in the anterior visual pathway at peak disease, without detectable reductions in local optic nerve T-cell infiltration or gliosis. This protection of visual function was not sustained after clinical symptom onset-initiated treatment paradigms and was observed alongside CHOP transcript and cleaved caspase-3 enrichment in the optic nerve at peak EAE. Together, these findings show that Sephin1 protects visual circuit function and structure during peak inflammatory demyelination, but is insufficient to prevent chronic visual impairment.

METHODS

Mice

Wild-type C57BL/6J mice (stock no. 000664) were obtained from The Jackson Laboratory and used for all experiments. Animals were housed under standard conditions on a 12-h light/12-h dark cycle with *ad libitum* access to food and water. Mice were 7–11 weeks old at the beginning of experimental procedures and were age-matched within each experimental cohort. Mice were randomly assigned to

treatment groups where applicable. All animal procedures were reviewed and approved by the University of Michigan Institutional Animal Care and Use Committee and were conducted in accordance with institutional and national guidelines for the care and use of laboratory animals.

Experimental Autoimmune Encephalomyelitis

Experimental autoimmune encephalomyelitis (EAE) was induced using an established myelin oligodendrocyte glycoprotein peptide (MOG_{35-55}) immunization protocol (40). 7-11-week-old mice were immunized subcutaneously at sites over the flanks of both hind limbs with 200 µg MOG_{35-55} peptide emulsified in Complete Freund's Adjuvant (CFA) containing heat-killed *Mycobacterium tuberculosis* H37Ra according to the manufacturer's formulation (Hooke Laboratories, MA, USA). Control mice received CFA injections prepared without MOG_{35-55} peptide. Pertussis toxin (150 ng) in phosphate-buffered saline (PBS) was administered to all mice intraperitoneally on the day of immunization and again 48 h later. Mice were weighed and clinically scored each day. Disease severity was scored using the following scale: 0.5, distal tail limpness; 1, complete limp tail; 1.5, limp tail with hindlimb weakness; 2, mild hindlimb paresis; 2.5, unilateral hindlimb paralysis; 3, bilateral hindlimb paralysis; and 4, moribund. Tissue was collected for analysis at peak disease (17 dpi) or at chronic disease (30 dpi). No CFA-injected control animal developed clinical symptoms, and no EAE mouse reached a score of 4 in this study.

Sephin1 treatment

Sephin1 (Millipore Sigma, SML1356) was dissolved in dimethyl sulfoxide (DMSO) to generate a stock solution and stored at − 20°C. Immediately before injection, Sephin1 was diluted in sterile 0.9% saline or 1x PBS to a final DMSO concentration of 1%. Mice received Sephin1 at 8 mg/kg or vehicle containing an equivalent volume of 1% DMSO by intraperitoneal injection once daily. For prophylactic-to-peak disease experiments, treatment began at 7 dpi and continued until tissue collection at 17 dpi. For therapeutic treatment beginning at the onset of disease, Sephin1 administration began at the first appearance of clinical signs and continued either until 30 dpi (chronic treatment) or for 7 days (abbreviated treatment), as indicated. Treatment groups were randomized, and investigators were blinded to treatment group during behavioral testing, electrophysiological recordings, imaging, and quantification.

Tissue preparation

At the designated experimental endpoints, mice were deeply anesthetized with a lethal intraperitoneal injection of Avertin and transcardially perfused with 0.1 M phosphate buffer (PB), followed by 4% paraformaldehyde (PFA) in 0.1 M PB. Brains, eyes, and optic nerves were carefully dissected and post-fixed in 4% PFA for 4 h at 4°C. Following fixation, tissue was cryoprotected in 30% sucrose prepared in 0.1 M PB at 4°C until equilibrated. Tissue was then embedded in a 1:1 mixture of 30% sucrose/PB and Optimal Cutting Temperature (O.C.T., 23-730-571, Fisher Scientific, Waltham, MA) compound. Coronal

brain sections and longitudinal optic nerve sections were cut at 10 µm, and retinal cross sections were sliced at 20 µm using a cryostat. Serial sections were collected to sample central areas of the dorsal LGN, the entire optic nerve, and retinal sections around the optic nerve head. Sections were then mounted onto slides for subsequent immunostaining.

Immunohistochemistry

Immunofluorescent staining was performed on tissue sections as follows: Sections were first washed in 0.1 M PB and then blocked and permeabilized for 1 h at room temperature in blocking buffer containing 10% normal horse serum and 0.6% Triton X-100 in 0.1 M PB. The following primary antibodies were diluted in blocking solution and applied overnight at room temperature: rabbit anti-CD3 (abcam, ab16669, 1:500, RRID: AB_443425), rat anti-CD45 (Bio-Rad, MCA1388, 1:200, RRID: AB_321729), rabbit anti-cleaved caspase-3 (R&D Systems, MAB835, 1:1000, RRID: AB_2243951), rat anti-Clec7a (InvivoGen, mabg-mdect, 1:200, RRID: AB_2753143), rabbit anti-phospho-eIF2α/eIF2S1, Ser51 (phosphorylated eIF2α, abcam, ab32157, 1:500, RRID: AB_732117), rabbit anti-G3BP1 (abcam, ab181150, 1:500, RRID: AB_2847886), mouse anti-GFAP (Sigma, G3893, 1:1000, RRID: AB_477010), rabbit anti-Homer1 (Synaptic Systems, 160003, 1:500, RRID: AB_887730), rat anti-MBP (EMD Millipore, MAB386, 1:500, RRID: AB_94975), rabbit anti-neurofilament 200 (Sigma-Aldrich, N4142, 1:1000, RRID: AB_477272), rabbit anti-P2RY12 (AnaSpec, AS-55043A, 1:2000, RRID: AB_2298886), rabbit anti-RBPMS (Proteintech, 15187-1-AP, 1:300, RRID: AB_2238431), guinea pig anti-TMEM119 (Synaptic Systems, 400004, 1:500, RRID: AB_2744645), goat anti-TPPP (Thermo Fisher Scientific, PA5-19243, 1:200, RRID: AB_10979400), guinea pig anti-VGluT2 (Synaptic Systems, 135404, 1:2000, RRID: AB_887884). The following day, sections were washed thoroughly in 0.1 M PB and incubated for 1 h at room temperature with species-appropriate Alexa Fluor–conjugated secondary antibodies (Thermo Fisher Scientific, 1:1000). After washing unbound antibody in 0.1 M PB, sections were coverslipped with Fluoromount-G™ (0100–01, SouthernBiotech, Birmingham, AL) containing 1:1000 Hoechst (H1398, Thermo Fisher Scientific, Waltham, MA) to counterstain nuclei.

RNA in situ hybridization

RNA *in situ* hybridization was performed according to the manufacturer's instructions using the RNAscope platform (ACDBio, Newark, CA). Briefly, optic nerve, retinal, or LGN-containing sections from each sample were treated with Protease III for 20 min at 40°C, rinsed in RNase-free water, and hybridized with a pre-validated probe targeting *Ddit3* (ACDbio, 317661, NM_007837.3) for 2 h at 40°C. Signal amplification steps were then carried out according to the manufacturer's protocol. Sections were washed and coverslipped with Fluoromount-G™ (0100–01, SouthernBiotech, Birmingham, AL) containing 1:1000 Hoechst (H1398, Thermo Fisher Scientific, Waltham, MA) to counterstain nuclei.

Confocal microscopy

Fluorescently-labeled sections were imaged using a Zeiss LSM900 laser-scanning confocal microscope equipped with 405, 488, 561, and 640 nm laser lines and controlled with ZEN Blue v3.7 software. For each staining experiment, imaging parameters were established using representative sections and then held constant across all animals and treatment groups within that experiment. Images were acquired using a 20x objective for regional area and cell-count analyses and a 63x objective for synaptic density and RNA *in situ* analyses. When z-stacks were collected, optical section spacing of 1.0 µm and stack depth of three or five planes were kept consistent across samples within each experiment. Maximum projections were generated for image area analysis, and separate planes were averaged for synaptic density analysis. Representative images were generated from maximum projections. All images used for quantitative analysis were acquired under non-saturating conditions.

Image processing and threshold-based quantification

Image analysis was performed using Fiji/ImageJ (NIH; v1.54k) by investigators blinded to experimental condition. For each marker, images were processed using a consistent workflow within each experiment. Briefly, images were background-subtracted and converted as needed for threshold-based analysis. Threshold parameters were determined from representative images spanning the experimental conditions and then applied uniformly to all images from the same staining experiment. Regions of interest (ROIs) were delineated using nuclei morphology, relevant immunostaining patterns, or anatomical landmarks. For threshold-based measurements, binary masks were generated from the processed images, and the area occupied by threshold-positive signal was quantified using the 'Analyze Particles' or 'Measure' functions in Fiji/ImageJ. For each animal, values from technical replicates as indicated below, including sections, fields of view, or z-planes, were averaged to generate a single biological value per animal for each ROI and marker. Quantification was performed with the average values for each animal as the primary biological unit.

Myelin, axonal, astrocyte, and microglial marker area analysis

Myelin, axonal, and glial markers were quantified on sections containing the retina, optic nerve, or LGN. For each animal, two to four sections were immunostained and imaged using identical acquisition parameters across groups. Four to twelve fields of view were acquired per region, depending on tissue size and sampling strategy, and analyses were performed in Fiji/ImageJ under blinded conditions as described above. MBP, NF200, GFAP, Clec7a, and P2RY12 immunoreactivity were quantified as the percentage of ROI area occupied by threshold-positive signal. Images were background-subtracted and manually thresholded using marker-specific parameters that were applied uniformly across all samples within an experiment. Measurements from all sections and fields of view were averaged to generate one value per animal for each region analyzed.

Myeloid, oligodendrocyte, RGC, and apoptotic marker cell counts

CD3, CD45^{hi}, TPPP, RBPMS, and cleaved caspase-3^{+} cells were counted for each field of view for the relevant tissue region in Fiji/ImageJ by an investigator blinded to experimental condition and normalized to ROI area. Counts from two to four sections and four to twelve fields of view, depending on tissue size and sampling strategy, were averaged to generate one value per animal for each region analyzed.

Synaptic density and in situ Ddit3 puncta analysis

Synaptic terminal density was assessed by quantifying vesicular glutamate transporter 2 (VGluT2)$^{+}$-presynaptic retinal ganglion cell terminals and Homer1^{+}-postsynaptic densities in the LGN. For each animal, 63x confocal images were collected from six non-overlapping fields of view per region (two to four sections). Z-stacks containing five optical planes were acquired with uniform spacing and imaging settings across all samples. Images were analyzed in Fiji/ImageJ by an investigator blinded to experimental group. Individual optical planes were background-subtracted and thresholded using a single thresholding approach for each experiment. VGluT2- or Homer1- positive synaptic puncta were quantified as the percentage of ROI area occupied by threshold-positive signal. Structural synapses were defined as colocalized pre- and postsynaptic markers (VGluT2^{+}/Homer1^{+} area). Values were averaged across z-planes, fields of view, and sections to generate a single synaptic density value per animal for each region. For *Ddit3*$^{+}$ *in situ* hybridization puncta quantification, 63x (LGN and optic nerve) or 20x (retina) images were collected from four to twelve non-overlapping fields of view per region (two to four sections). Z-stacks containing three optical planes were acquired with uniform spacing and imaging settings across all samples. Maximum projections were generated for quantification, and images were background-subtracted and thresholded manually by an investigator blinded to experimental condition. *Ddit3*$^{+}$ puncta were quantified as the percentage of ROI area occupied by threshold-positive signal. Fields of view were averaged to generate a single puncta area value per animal for each region.

Optomotor response testing

Visual function was assessed using the OptoMotry system (CerebralMechanics, Medicine Hat, AB, Canada). Mice were tested while awake and freely moving, without prior training required (38, 40). Each animal was placed on an elevated platform positioned in the center of a chamber surrounded by four computer monitors displaying visual stimuli. Stimuli consisted of a virtual rotating cylinder of vertical sine-wave gratings presented at 100% contrast and a rotation speed of 12°/s. Spatial frequency and rotation direction were varied systematically to determine visual acuity scores. Reflexive head-tracking movements in response to the rotating gratings were recorded with an overhead camera and scored by an observer blinded to the experimental condition. Visual acuity was defined as the highest spatial frequency, reported in cycles per degree, that reliably elicited head tracking. Acuity thresholds were determined separately for each eye based on rotation direction and averaged to generate one value per animal. Testing was performed at baseline and at defined experimental endpoints, including peak and

chronic EAE. For longitudinal experiments, baseline and post-treatment values were compared within animals when appropriate.

Pattern VEP/ERG

Pattern-stimulated visual evoked potentials (pVEP) and electroretinograms (PERG) were recorded following optomotor response assessments at baseline and peak EAE (16 dpi). Mice were dark-adapted for 3 h prior to testing, and all recordings were performed in a dark room. Mice were anesthetized with ketamine (100 mg/kg) and xylazine (10 mg/kg), and anesthetic depth was confirmed by the absence of a toe-pinch response. Pupils were dilated using 0.5% tropicamide (Hilco, 1029321, Northbrook, IL) and 2.5% phenylephrine hydrochloride (Hilco, 1307622, Northbrook, IL), and 0.5% proparacaine eye drops (Accutome, AX0502, Malvern, PA) were administered as a topical anesthetic. GenTeal (0.3% Hypromellose, Alcon, Fort Worth, TX) was used to lubricate the eyes. pVEPs and PERGs were recorded simultaneously on a Celeris™ device (Diagnosys LLC, Lowell, MA, USA). Pattern stimuli were presented through corneal stimulators with integrated recording electrodes at 100% contrast, a spatial frequency of 0.059 cycles/degree, luminance of 50 cd/m^2, and alternating at 2.1 reversals/second. A total of 300 sweeps were collected per run. pVEPs were recorded using an active electrode positioned subcutaneously over the visual cortex, a reference electrode placed in the cheek, and a ground electrode placed at the base of the tail. PERGs were recorded from the corneal electrodes. Amplitudes and latencies were calculated for the dominant pVEP N1 response and the PERG P1 and N2 responses. Values from both eyes were averaged to generate a single value per animal.

Statistical analysis

Statistical analyses were performed using GraphPad Prism version 11.0.0 (GraphPad Software). Data are presented as mean ± standard error of the mean (SEM). The number of biological replicates, relevant statistical test, and all *P* values are reported in the corresponding figure legends, with individual animals considered the primary biological unit for all experiments. For comparisons between two independent groups, two-tailed unpaired Student's t-tests were used when data met parametric assumptions. For comparisons involving more than two groups, one-way ANOVA followed by Tukey's multiple-comparisons test was used, and two-way ANOVA with Tukey's multiple-comparisons test was used to analyze multiple groups across multiple time points. Correlations were assessed using a simple linear regression, and R-squared values are reported in the figure and figure legend. Non-significant results are reported as ns ($p \geq 0.05$). Statistical significance was defined as $p < 0.05$.

RESULTS

Prophylactic Sephin1 treatment preserves visual function at peak EAE

To first assess whether treatment with Sephin1 affects visual circuit function, we performed visual assessments including testing the optomotor response and recording pVEPs and PERGs at baseline and

at peak EAE (16 days post-induction, dpi, Fig. 1A). Sephin1 (8 mg/kg) or vehicle (1% DMSO) was administered prophylactically (beginning at 7 dpi, before the onset of EAE clinical symptoms) by daily intraperitoneal injection until the experimental endpoint (17 dpi, Fig. 1A). Consistent with previous reports showing that prophylactic Sephin1 treatment attenuates EAE severity during peak EAE (24), mice treated with Sephin1 (EAE^{Seph}) had a significantly lower final clinical score at 17 dpi than vehicle-treated EAE mice (EAE^{Veh}, Fig. 1B). Optomotor responses, reported as visual acuity in cycles/degree (c/d), were similar across all experimental groups at baseline (prior to EAE induction, Fig. 1C). At peak EAE (16 dpi), EAE^{Veh} mice had significantly lower visual acuity than control mice treated with Complete Freund's Adjuvant (CFA) and Sephin1 (CFA^{Seph}), similar to previous reports showing reduced visual acuity during EAE (40, 41). EAE^{Seph} mice had preserved visual acuity relative to EAE^{Veh} mice (Fig. 1C), and this protection was also observed when peak visual acuity was normalized to each animal's baseline value (Figure S1A). Of note, Sephin1 treatment did not alter visual acuity in the absence of EAE, as shown by no change from baseline values in CFA^{Veh} versus CFA^{Seph} mice (Figure S1B). In addition, Sephin1 alone did not alter weight (Figure S1C) or hallmark features in the visual thalamus (lateral geniculate nucleus, LGN) of CFA mice, including neurofilament 200^{+} axon density (NF200, Figure S1D-E), myelin basic protein density (MBP, Figure S1F-G), or immunoreactivity of astrocyte and microglia markers (GFAP and P2RY12, Figure S1H-I and S1J-K, respectively). Therefore, CFA^{Seph} mice were used for all subsequent statistical comparisons as indicated.

EAE^{Seph} mice still had significantly reduced visual acuity relative to CFA^{Seph} mice (Fig. 1C), indicating that treatment with Sephin1 does not fully protect visual function, reminiscent of incompletely attenuated EAE clinical scores. Indeed, visual acuity strongly correlated with final EAE clinical scores across experimental groups regardless of pharmaceutical treatment, suggesting that visual dysfunction tracks overall EAE disease severity (Fig. 1D). To further investigate function across the visual pathway, pVEP responses were recorded above the visual cortex. Recordings showed a prominent negative waveform characteristic of the pVEP that was maintained across all experimental groups (Fig. 1E). The amplitude of the negative response (N1), expressed relative to baseline, was significantly reduced in EAE^{Veh} mice compared to both CFA^{Seph} and EAE^{Seph} mice (Fig. 1F). In contrast, N1 amplitude was largely preserved in EAE^{Seph} mice, and was not statistically different from CFA^{Seph} responses, suggesting preservation of visually evoked cortical response magnitude. At this disease time point, response latency did not differ significantly across groups (Figure S2A), demonstrating that peak EAE primarily reduced pVEP amplitude rather than producing a detectable latency shift.

PERG responses were also recorded to test RGC function, which manifests as a positive peak (P1) followed by a negative response (N2) (42) (Figure S2B). PERG amplitude was not altered across groups for the total P1-N2 response (Figure S2C), nor were amplitudes or latencies statistically different for the individual P1 and N2 responses (Figure S2D-G). As the PERG is recorded at the cornea and specific to RGC function, these results were consistent with unchanged numbers of $RBPMS^{+}$ RGCs in the ganglion cell layer (GCL, Figure S2H-I) at peak EAE and with literature showing that RGCs are not lost until the

chronic stage of EAE (43–45). Qualitatively, the overall structure of the retina, including the GCL, inner plexiform layer (IPL), inner nuclear layer (INL), outer plexiform layer (OPL), and outer nuclear layer (ONL), also appeared unchanged (Figure S2H). Together, these results indicate that treatment with Sephin1 partially protects visual acuity, which correlates with overall EAE clinical severity, and robustly preserves pVEP response amplitude at peak EAE.

Sephin1 protects retinogeniculate axons, myelin, and synapses

To determine the histological pathologies associated with altered visual function, we assessed axons, myelin, and oligodendrocytes in the optic nerve, a key region of the anterior visual pathway targeted during EAE (Figure S3A). Low-magnification (10x) overview imaging of the optic nerves qualitatively showed preservation of $NF200^{+}$ axons in EAE^{Seph} mice compared to EAE^{Veh} mice (Figure S3B). Consistent with this, MBP^{+} myelin immunoreactivity was significantly reduced in EAE^{Veh} optic nerves but preserved in EAE^{Seph} optic nerves relative to CFA^{Seph} controls (Figure S3C-D). This was accompanied by partial preservation of the number of $TPPP^{+}$ myelinating oligodendrocyte cell bodies (number/100 microns) in EAE^{Seph} mice compared to EAE^{Veh} mice, although $TPPP^{+}$ cells remained significantly reduced relative to CFA^{Seph} controls (Figure S3E-F). The persistence of reduced $TPPP^{+}$ oligodendrocyte numbers despite preserved MBP immunoreactivity suggests that oligodendrocyte cell body loss may be detectable before more extensive loss of myelin signal at this disease stage.

To confirm these results, 20x images were acquired from smaller fields of view along the optic nerve. Both $NF200^{+}$ axon and MBP^{+} myelin densities were significantly reduced in EAE^{Veh} mice compared to CFA^{Seph} controls and EAE^{Seph} mice (Fig. 2A-D). In contrast, EAE^{Seph} mice were not statistically different from CFA^{Seph} controls for either $NF200^{+}$ axon or MBP^{+} myelin densities in the optic nerve (Fig. 2A-D). Consistent with the low-magnification analysis (Figure S3E,F), $TPPP^{+}$ oligodendrocytes density were significantly reduced in both EAE^{Veh} and EAE^{Seph} mice compared to CFA^{Seph} controls, but EAE^{Seph} mice had significantly higher numbers of $TPPP^{+}$ cells than EAE^{Veh} mice (Fig. 2E,F).

To determine whether preservation of RGC axons projecting through the optic nerve was accompanied by preservation of their downstream retinogeniculate synaptic terminals, we assessed axonal and synaptic markers in the LGN (Fig. 3A). Similar to the optic nerve, $NF200^{+}$ axon density was preserved in EAE^{Seph} mice compared to EAE^{Veh} mice, and was not

statistically different from CFA^{Seph} controls (Fig. 3B-C). $VGluT2^{+}$ RGC presynaptic terminals in the LGN were also significantly protected in EAE^{Seph} mice compared to EAE^{Veh} mice and were not statistically altered compared to CFA^{Seph} controls (Fig. 3D-E). To determine if postsynaptic densities were changed and assess structural synapses, the postsynaptic marker Homer1 was analyzed alongside VGluT2. $Homer1^{+}$ postsynaptic densities were not altered across any experimental groups (Fig. 3F-G), suggesting that retinogeniculate presynaptic terminals are more vulnerable than $Homer1^{+}$ postsynaptic structures at

this disease stage. This is consistent with evidence of predominant presynaptic terminal loss at onset and peak EAE (40, 44). To assess whether preservation of VGluT2 is accompanied by protection of structural synapses (containing pre- and postsynaptic densities), we measured the colocalization of $VGluT2^{+}$ and $Homer1^{+}$ signals. EAE^{Veh} mice had significantly reduced structural synapses compared to CFA^{Seph} controls (Fig. 3H-I). In EAE^{Seph} mice, VGluT2/$Homer1^{+}$ colocalized area was not statistically different from CFA^{Seph} controls and was significantly preserved relative to EAE^{Veh} mice (Fig. 3I). Together, these results show that Sephin1 protects optic nerve axons and myelin and preserves downstream retinogeniculate synapses in the LGN at peak EAE.

Sephin1 does not reduce local inflammation or gliosis in the anterior visual pathway

We next assessed whether the functional and structural protection we observed in EAE^{Seph} mice could be explained by reduced inflammation, as Sephin1 has been previously reported to reduce accumulation of infiltrating immune cells in the spinal cord (24). In the optic nerve, $CD45^{+}$ immune cells and $CD3^{+}$ T cells were significantly increased in EAE^{Veh} mice compared to CFA^{Seph} controls, as expected after EAE induction (Fig. 4A-D). Different from the spinal cord, EAE^{Seph} mice showed comparable numbers of $CD45^{+}$ and $CD3^{+}$ cells relative to EAE^{Veh} mice in the optic nerve, and both EAE groups were significantly increased compared with CFA^{Seph} controls (Fig. 4A-D). Thus, Sephin1 did not detectably reduce immune cell infiltration to the optic nerve at peak EAE.

To further interrogate potential changes in the local inflammatory milieu, we assessed astrocyte and microglial responses across experimental groups. In the optic nerve, $GFAP^{+}$ astrocyte immunoreactivity was significantly increased in both EAE^{Veh} and EAE^{Seph} mice compared to CFA^{Seph} controls, with no difference between the two EAE groups (Fig. 4E-F). Similar results were observed for $Clec7a^{+}$ disease-associated microglia immunoreactivity, which was increased in both EAE groups relative to CFA^{Seph} controls, but was not significantly different between EAE^{Veh} and EAE^{Seph} mice (Fig. 4G-H). Comparable glial responses were also observed downstream of the optic nerve in the LGN, where $GFAP^{+}$ and $Clec7a^{+}$ immunoreactivity were significantly increased in both EAE^{Veh} and EAE^{Seph} mice compared to CFA^{Seph} controls, but did not differ between the two EAE groups (Figure S4A-D). Additionally, to determine whether the overall microglial coverage was altered in the LGN, we assessed TMEM119 immunoreactivity, which was increased in EAE mice compared with CFA^{Seph} controls but was not significantly different between EAE^{Veh} and EAE^{Seph} mice (Figure S4E-F). Overall, these findings suggest that typical inflammatory responses occurred similarly across vehicle- and Sephin1-treated EAE mice within the anterior visual pathway, suggesting that Sephin1-mediated protection is not explained by detectable reductions in local inflammation.

Sephin1 enhances ISR-associated stress signaling in the optic nerve at peak EAE

Although visual function is preserved at peak EAE, previous work has demonstrated that Sephin1-mediated protection against clinical severity or histological pathology is not sustained past this stage in the spinal cord (24). Because Sephin1 has been reported to prolong ISR signaling by maintaining elevated phosphorylation of eIF2α under stress, we next assessed markers of cellular stress signaling in the anterior visual pathway. In the optic nerve, p-eIF2α^{+} immunoreactivity was significantly increased in EAE^{Seph} mice compared to EAE^{Veh} mice and CFA^{Seph} controls (Fig. 5A-B), indicating enhanced ISR-associated signaling in the optic nerve only after Sephin1 treatment. Phosphorylation of eIF2α suppresses global translation and is associated with the formation of stress granules, which can be labeled by G3BP1 (46, 47). We therefore assessed G3BP1^{+} stress granules as an indicator of ISR activation in the GCL of the retina. G3BP1^{+} immunoreactivity was highest in EAE^{Seph} mice and was significantly increased relative to CFA^{Seph} controls, although it was not significantly different from EAE^{Veh} mice (Fig. 5C,D). In the LGN, G3BP1^{+} area was significantly increased in both EAE^{Veh} and EAE^{Seph} mice compared to CFA^{Seph} controls, with no statistical difference between the EAE groups (Fig. 5E-F). Together, these data indicate that Sephin1 treatment is associated with increased p-eIF2α signaling in the optic nerve, whereas G3BP1-associated stress responses in the retina and LGN appear to be influenced by EAE and are not uniquely increased by Sephin1.

Because sustained ISR signaling can promote induction of CHOP, encoded by *Ddit3*, and CHOP has been linked to apoptotic pathways (21–23), we next assessed whether *Ddit3* mRNA was increased in the anterior visual pathway. Using RNA *in situ* hybridization, we found that *Ddit3*$^{+}$ puncta were significantly increased in the optic nerve of EAE^{Seph} mice compared to both EAE^{Veh} mice and CFA^{Seph} controls (Fig. 6A-B). EAE^{Veh} mice also showed a trend toward increased *Ddit3*$^{+}$ puncta compared to CFA^{Seph} controls (Fig. 6B). Consistent with increased stress-associated signaling in the optic nerve, cleaved caspase-3 (cCasp3)$^{+}$ apoptotic cells were increased in EAE^{Seph} optic nerves compared to CFA^{Seph} controls (Fig. 6C-D). Similar to *Ddit3* mRNA, cCasp3^{+} apoptotic cells also trended upward in EAE^{Veh} mice compared with CFA^{Seph} controls (Fig. 6C). In contrast to the optic nerve, *Ddit3* was not significantly altered across experimental groups in the retina or LGN (Figure S5A-D). Together, these results suggest that Sephin1-treated EAE optic nerves show enhanced CHOP-associated stress signaling, which may contribute to the limited durability of Sephin1-mediated protection.

Onset-initiated Sephin1 treatment fails to preserve visual function

To determine whether the timing of Sephin1 treatment impacts the durability of visual protection in a therapeutically relevant setting, we tested two additional treatment paradigms during EAE.

First, Sephin1 or vehicle treatment was initiated at the onset of clinical symptoms and continued until chronic EAE (30 dpi). This treatment method had been previously suggested to increase remyelination at chronic EAE in the spinal cord (28). Under this paradigm, visual acuity was significantly decreased at the chronic time point in both EAE^{Veh} and EAE^{Seph} mice compared to CFA^{Seph} controls, with no differences

between the two EAE groups (Fig. 6E). Second, to determine whether a shorter onset-initiated treatment course was sufficient to preserve visual function, Sephin1 or vehicle was administered beginning at clinical onset for 7 days only, and visual acuity was assessed at the chronic EAE time point. Again, visual acuity was reduced in both EAE groups relative to CFA^{Seph} controls, and did not differ between EAE^{Veh} and EAE^{Seph} mice (Fig. 6F). Together, these findings indicate that onset-initiated Sephin1 treatment, whether sustained through chronic disease or limited to 7 days, is insufficient to preserve chronic visual function, suggesting that Sephin1-mediated visual protection is constrained by treatment timing and disease stage.

DISCUSSION

Our study shows that prophylactic treatment with Sephin1 preserves optomotor visual acuity, pVEP amplitudes, and the integrity of the retinogeniculate circuit at peak EAE. Previous evidence for the functional benefit of Sephin1 in inflammatory demyelination was limited to spinal cord-driven motor deficits (24), which are not as structurally distinct or as sensitive for detecting subtle circuit-specific changes as the visual pathway. Thus, it was previously unclear whether Sephin1 provided neuroprotection to defined neural circuits during EAE. Although the optomotor response has been established to reliably detect functional changes in EAE (40, 41, 48), because these responses are influenced by motor ability (38, 49), which is impaired in EAE, the preservation of pVEP amplitudes provides important complementary electrophysiological evidence that Sephin1 protects visual pathway function. While PERG responses were unchanged, these results are consistent with our observations and previous literature showing

that RGC function is primarily affected during the chronic stage of disease rather than at peak EAE (43–45). Together, the preservation of optomotor visual acuity and pVEP amplitudes, in the absence of detectable PERG changes, suggests that Sephin1 preserves visual pathway function during peak EAE without adversely affecting RGC function.

In addition to our functional observations, we found that Sephin1 preserved myelin, axons, and oligodendrocytes in the optic nerve, and retinogeniculate synapses in the LGN. The protection of these synapses may reflect, at least in part, maintained optic nerve axonal and myelin integrity, though direct effects of Sephin1 on LGN synapses cannot be excluded. The preservation of myelin and axonal integrity in the optic nerve was consistent with protection previously reported in the spinal cord at peak EAE with Sephin1 treatment (24). However, studies in the spinal cord also showed a delay in the T cell-driven inflammatory response that is characteristic of EAE, suggesting that Sephin1 partly ameliorated clinical severity by reducing overall autoimmune inflammation during peak disease (24). In the optic nerve, we did not observe a change in the numbers of $CD3^{+}$ T cells or $CD45^{hi+}$ myeloid cells at peak EAE. Although these data do not allow us to determine whether the activation states of these cells were similar between EAE^{Veh} and EAE^{Seph} mice, the level of peripheral immune cell infiltration stands in contrast to what has been reported in the spinal cord. In line with these results, we also observed similar levels of

reactive astrocytes and microglia, suggesting that the protection of the retinogeniculate circuit was not explained by a reduction in inflammatory cell infiltration or gliosis at peak EAE.

As Sephin1 sustains p-eIF2α levels by inhibiting its dephosphorylation (24, 26), we investigated components of p-eIF2α signaling in the retinogeniculate pathway. We found that, specifically in the optic nerve, Sephin1 increased both p-eIF2α and *Ddit3*, which encodes CHOP, a downstream target of ISR activation (50). Since sustained CHOP activation can induce apoptotic pathways, these findings raise the possibility that Sephin1 may become maladaptive rather than protective, a possibility supported by our data showing an increase in the number of cleaved caspase-3^{+} cells in the optic nerve. Of note, we observed a significant increase in stress granules, a marker of cellular stress tightly associated with ISR activation (47, 51), equally in EAE^{Veh} and EAE^{Seph} mice compared to controls in the LGN. This suggests that EAE induces cellular stress responses in the LGN, but that Sephin1-associated effects on ISR signaling may be more pronounced in primary white matter than gray matter. The increase in stress granules in the LGN was not accompanied by an increase in *Ddit3*, suggesting that stress responses in the LGN do not necessarily follow the same pattern observed in the optic nerve.

Consistent with the possibility that the protective effects of Sephin1 are temporally restricted and may become maladaptive, previous studies in the spinal cord have shown that protection against demyelination and axon loss is not maintained during chronic EAE, despite early protection when Sephin1 is administered prophylactically (24). However, there is also evidence suggesting that treatment beginning at the onset of EAE clinical symptoms can promote remyelination (28). We therefore investigated whether Sephin1 treatment beginning at EAE onset was sufficient to preserve visual function. However, Sephin1 did not alter visual acuity during chronic EAE when administered from the onset of clinical symptoms through 30 dpi, nor when treatment was abbreviated to the first 7 days after EAE onset. These findings suggest that Sephin1 has a limited therapeutic window for preserving visual function during EAE. One possibility is that visual pathway pathology is too pronounced by the onset of clinical motor symptoms, limiting the efficacy of delayed treatment. Additionally, any potential enhancement of remyelination that may occur under these treatment conditions was not sufficient to produce a detectable functional improvement in the visual pathway.

Together, our data suggest that Sephin1-associated preservation of visual function at peak EAE is most closely associated with protection of white matter pathology in the optic nerve, including preservation of myelin, axons, and oligodendrocytes. The ISR and the effects of Sephin1 have been extensively studied in oligodendrocytes, providing evidence that this cell population can benefit, at least transiently, from enhanced ISR activation during inflammatory demyelination (24, 28, 30). While we did not evaluate cell-specific effects in the retinogeniculate pathway, the prominent protection observed in the optic nerve, the lack of Sephin1-specific functional effects in the retina, the absence of Sephin1-mediated ISR changes in the LGN, and the lack of changes in inflammatory cell infiltration and gliosis, suggest that oligodendrocytes may also be a primary cell affected in our study at peak EAE. Future work will investigate this possibility and define the cell-specific mechanisms that may explain the lack of visual function improvement following therapeutic Sephin1 treatment. Additionally, evidence that RGCs can be

protected during EAE when ISR signaling is genetically inhibited (52) highlights the possibility that ISR activation has divergent effects depending on cell type, CNS region, and disease stage. These findings warrant further investigation into the spatiotemporal and cell-specific effects of ISR modulation and its potential as a therapeutic target for neuroprotection in inflammatory demyelinating disease.

CONCLUSIONS

Our results show that prophylactic Sephin1 treatment preserves visual function at peak EAE, including visual acuity and pVEP response amplitude. This functional protection was accompanied by preservation of optic nerve axons, myelin, and oligodendrocyte cell bodies, as well as protection of structural retinogeniculate synapses in the LGN. These protective effects occurred despite comparable local immune infiltration, astrogliosis, and microglial responses in vehicle- and Sephin1-treated EAE mice, suggesting that Sephin1-mediated visual pathway protection is not explained by reductions in local inflammation. Sephin1-mediated protection has previously been shown to be transient, and our data indicate that downstream stress signals associated with apoptotic pathway activation are increased in the optic nerves of Sephin1-treated EAE mice. These stress-associated signaling changes may contribute to the limited durability of Sephin1-mediated protection. Consistent with this possibility, visual function was not protected during chronic EAE when Sephin1 treatment was initiated after the onset of clinical symptoms, regardless of whether treatment was continued until chronic disease or limited to a shortened 7-day course. Together, these data suggest that while Sephin1 can protect visual circuit structure and function during peak EAE, its protective effect on the visual circuit is temporally limited and is not sufficient to prevent chronic visual dysfunction.

Abbreviations

CFA
Complete Freund’s adjuvant
CFA^{Seph}
Sephin1-treated CFA control mice
CFA^{Veh}
Vehicle-treated CFA control mice
cCasp3
Cleaved caspase-3
CD3
Cluster of differentiation 3
CD45
Cluster of differentiation 45
CHOP
C/EBP homologous protein
CNS

Central nervous system
Ddit3
DNA damage-inducible transcript 3
dpi
Days post-induction
DMSO
Dimethyl sulfoxide
EAE
Experimental autoimmune encephalomyelitis
EAE^{Seph}
Sephin1-treated EAE mice
EAE^{Veh}
Vehicle-treated EAE mice
eIF2α
Eukaryotic translation initiation factor 2 alpha
eIF2B
Eukaryotic translation initiation factor 2B
G3BP1
Ras GTPase-activating protein-binding protein 1
GADD34
Growth arrest and DNA damage-inducible protein 34
GCL
Ganglion cell layer
GFAP
Glial fibrillary acidic protein
IFN-γ
Interferon gamma
INL
Inner nuclear layer
IPL
Inner plexiform layer
ISR
Integrated stress response
LGN
Dorsal lateral geniculate nucleus
MBP
Myelin basic protein
$MOG_{35–55}$
Myelin oligodendrocyte glycoprotein peptide 35–55
MS

Multiple sclerosis
NF200
Neurofilament 200
OMR
Optomotor response
ON
Optic nerve
ONL
Outer nuclear layer
OPL
Outer plexiform layer
PB
Phosphate buffer
PBS
Phosphate-buffered saline
PERG
Pattern electroretinogram
PFA
Paraformaldehyde
p-eIF2α
Phosphorylated eukaryotic translation initiation factor 2 alpha
pVEP
Pattern-stimulated visual evoked potential
P2RY12
Purinergic receptor P2Y12
RBPMS
RNA-binding protein with multiple splicing
RGC
Retinal ganglion cell
ROI
Region of interest
SEM
Standard error of the mean
TPPP
Tubulin polymerization-promoting protein
VGluT2
Vesicular glutamate transporter 2

Declarations

ETHICS APPROVAL AND CONSENT TO PARTICIPATE

All animal procedures were approved by the University of Michigan Institutional Animal Care and Use Committee under IACUC protocols PRO00011096 and PRO00012631 (S.W.) and were performed in accordance with institutional guidelines for animal welfare. No human participants, human data, or human tissue specimens were used in this study.

AVAILABILITY OF DATA AND MATERIALS

All data supporting the findings of this study are included in the manuscript and supplementary materials. Additional raw data and analysis files are available from the corresponding author upon request.

CONSENT FOR PUBLICATION

All authors reviewed and edited the manuscript and approved the final version for publication.

COMPETING INTERESTS

The authors have no competing interests to declare.

FUNDING

This work was supported by National Multiple Sclerosis Society Career Transition Fellowships (TA-1905-34048 to S.W. and TA-2008-37043 to Y.C.) and a Research to Prevent Blindness Unrestricted Grant to the Department of Ophthalmology and Visual Sciences. We also would like to acknowledge funding from the Department of Defense Multiple Sclerosis Early Investigator Research Award MS240048 (G.M.M).

AUTHOR CONTRIBUTIONS

S.W. conceived, designed, and led the study, supervised the project, analyzed and interpreted data, conceptualized figures, provided resources, acquired funding, and wrote the manuscript with input from all co-authors. G.M.M performed experiments, imaging, functional testing, quantitative analyses, data interpretation, figure generation, and contributed to writing the manuscript. M.J.C. contributed to imaging, quantitative analysis, and manuscript revision. J.N.S. contributed to quantitative analysis, figure generation, and manuscript revision. Y.C. contributed to study design, experimental procedures, and manuscript revision. All authors reviewed and edited the manuscript and approved the final version.

ACKNOWLEDGEMENTS

We gratefully acknowledge the animals used in this study and recognize their contribution to advancing biomedical research. We also would like to thank Drs. Mark T. Milner and Ross Pelzel for critical reading of the manuscript. The project described was supported in part by Grant Number P30 EY007003 from

the National Eye Institute through the University of Michigan Vision Research Core. The content is solely the responsibility of the authors and does not necessarily represent the official views of the NIH.

AUTHORS' INFORMATION

G.M.M., M.J.C, J.N.S, and S.W. are affiliated with the Department of Ophthalmology and Visual Sciences at the University of Michigan. S.W. also holds affiliations with the Department of Molecular & Integrative Physiology and the Neuroscience Institute at the University of Michigan. Y.C. is affiliated with the Department of Biology at Loyola University Chicago. The authors have collective expertise in analyzing the integrated stress response pathway, visual system pathology and functional assessments, neuroimmune mechanisms, neurodegenerative pathology, and quantitative analysis in MS-relevant models. Relevant methodological expertise includes MS-relevant EAE paradigms, immunohistochemistry, confocal microscopy, optomotor response testing, VEP/ERG recordings, and computational bioimage analysis.

ENDNOTES

Not Available

References

1. Frohman EM, Racke MK, Raine CS (2006) Multiple sclerosis–the plaque and its pathogenesis. N Engl J Med 354(9):942–955
2. Dutta R, Trapp BD (2011) Mechanisms of neuronal dysfunction and degeneration in multiple sclerosis. Prog Neurobiol 93(1):1–12
3. Reich DS, Lucchinetti CF, Calabresi PA (2018) Multiple Sclerosis. N Engl J Med 378(2):169–180
4. Dargahi N, Katsara M, Tselios T, Androutsou ME, de Courten M, Matsoukas J et al (2017) Multiple Sclerosis: Immunopathology and Treatment Update. Brain Sci. ;7(7)
5. Hauser SL, Cree BAC (2020) Treatment of Multiple Sclerosis: A Review. Am J Med 133(12):1380–90e2
6. Rollot F, Casey R, Kerbrat A, Edan G, Le Page E, Vukusic S et al (2026) Progression independent of relapse and MRI activity and treatment strategies in multiple sclerosis. Brain
7. Weideman AM, Tapia-Maltos MA, Johnson K, Greenwood M, Bielekova B (2017) Meta-analysis of the Age-Dependent Efficacy of Multiple Sclerosis Treatments. Front Neurol 8:577
8. Dimitriou NG, Meuth SG, Martinez-Lapiscina EH, Albrecht P, Menge T (2023) Treatment of Patients with Multiple Sclerosis Transitioning Between Relapsing and Progressive Disease. CNS Drugs 37(1):69–92
9. Trapp BD, Nave KA (2008) Multiple sclerosis: an immune or neurodegenerative disorder? Annu Rev Neurosci 31:247–269

10. Franklin RJ, ffrench-Constant C, Edgar JM, Smith KJ (2012) Neuroprotection and repair in multiple sclerosis. Nat Rev Neurol 8(11):624–634
11. Way SW, Popko B (2016) Harnessing the integrated stress response for the treatment of multiple sclerosis. Lancet Neurol 15(4):434–443
12. Rodgers JM, Robinson AP, Miller SD (2013) Strategies for protecting oligodendrocytes and enhancing remyelination in multiple sclerosis. Discov Med 16(86):53–63
13. Franklin RJM, Ffrench-Constant C (2017) Regenerating CNS myelin - from mechanisms to experimental medicines. Nat Rev Neurosci 18(12):753–769
14. Pakos-Zebrucka K, Koryga I, Mnich K, Ljujic M, Samali A, Gorman AM (2016) The integrated stress response. EMBO Rep 17(10):1374–1395
15. Costa-Mattioli M, Walter P (2020) The integrated stress response: From mechanism to disease. Science. ;368(6489)
16. Harding HP, Novoa I, Zhang Y, Zeng H, Wek R, Schapira M et al (2000) Regulated translation initiation controls stress-induced gene expression in mammalian cells. Mol Cell 6(5):1099–1108
17. Walter P, Ron D (2011) The unfolded protein response: from stress pathway to homeostatic regulation. Science 334(6059):1081–1086
18. Lin W, Bailey SL, Ho H, Harding HP, Ron D, Miller SD et al (2007) The integrated stress response prevents demyelination by protecting oligodendrocytes against immune-mediated damage. J Clin Invest 117(2):448–456
19. Lin W, Harding HP, Ron D, Popko B (2005) Endoplasmic reticulum stress modulates the response of myelinating oligodendrocytes to the immune cytokine interferon-gamma. J Cell Biol 169(4):603–612
20. Kojima E, Takeuchi A, Haneda M, Yagi A, Hasegawa T, Yamaki K et al (2003) The function of GADD34 is a recovery from a shutoff of protein synthesis induced by ER stress: elucidation by GADD34-deficient mice. FASEB J 17(11):1573–1575
21. Tabas I, Ron D (2011) Integrating the mechanisms of apoptosis induced by endoplasmic reticulum stress. Nat Cell Biol 13(3):184–190
22. Li Y, Guo Y, Tang J, Jiang J, Chen Z (2014) New insights into the roles of CHOP-induced apoptosis in ER stress. Acta Biochim Biophys Sin (Shanghai) 46(8):629–640
23. Marciniak SJ, Yun CY, Oyadomari S, Novoa I, Zhang Y, Jungreis R et al (2004) CHOP induces death by promoting protein synthesis and oxidation in the stressed endoplasmic reticulum. Genes Dev 18(24):3066–3077
24. Chen Y, Podojil JR, Kunjamma RB, Jones J, Weiner M, Lin W et al (2019) Sephin1, which prolongs the integrated stress response, is a promising therapeutic for multiple sclerosis. Brain 142(2):344–361
25. Way SW, Podojil JR, Clayton BL, Zaremba A, Collins TL, Kunjamma RB et al (2015) Pharmaceutical integrated stress response enhancement protects oligodendrocytes and provides a potential multiple sclerosis therapeutic. Nat Commun 6:6532

26. Das I, Krzyzosiak A, Schneider K, Wrabetz L, D'Antonio M, Barry N et al (2015) Preventing proteostasis diseases by selective inhibition of a phosphatase regulatory subunit. Science 348(6231):239–242
27. Ransohoff RM (2012) Animal models of multiple sclerosis: the good, the bad and the bottom line. Nat Neurosci 15(8):1074–1077
28. Chen Y, Kunjamma RB, Weiner M, Chan JR, Popko B (2021) Prolonging the integrated stress response enhances CNS remyelination in an inflammatory environment. eLife 10:e65469
29. Rankin KA, Mei F, Kim K, Shen YA, Mayoral SR, Desponts C et al (2019) Selective Estrogen Receptor Modulators Enhance CNS Remyelination Independent of Estrogen Receptors. J Neurosci 39(12):2184–2194
30. Chen Y, Quan S, Patil V, Kunjamma RB, Tokars HM, Leisten ED et al (2023) Insights into the mechanism of oligodendrocyte protection and remyelination enhancement by the integrated stress response. Glia 71(9):2180–2195
31. Wong YL, LeBon L, Basso AM, Kohlhaas KL, Nikkel AL, Robb HM et al (2019) eIF2B activator prevents neurological defects caused by a chronic integrated stress response. Elife. ;8
32. Sidrauski C, Tsai JC, Kampmann M, Hearn BR, Vedantham P, Jaishankar P et al (2015) Pharmacological dimerization and activation of the exchange factor eIF2B antagonizes the integrated stress response. Elife 4:e07314
33. Mendel I, Kerlero de Rosbo N, Ben-Nun A (1995) A myelin oligodendrocyte glycoprotein peptide induces typical chronic experimental autoimmune encephalomyelitis in H-2b mice: fine specificity and T cell receptor V beta expression of encephalitogenic T cells. Eur J Immunol 25(7):1951–1959
34. Gold R, Linington C, Lassmann H (2006) Understanding pathogenesis and therapy of multiple sclerosis via animal models: 70 years of merits and culprits in experimental autoimmune encephalomyelitis research. Brain 129(Pt 8):1953–1971
35. Stromnes IM, Goverman JM (2006) Active induction of experimental allergic encephalomyelitis. Nat Protoc 1(4):1810–1819
36. Balcer LJ, Miller DH, Reingold SC, Cohen JA (2015) Vision and vision-related outcome measures in multiple sclerosis. Brain 138(Pt 1):11–27
37. Green AJ, McQuaid S, Hauser SL, Allen IV, Lyness R (2010) Ocular pathology in multiple sclerosis: retinal atrophy and inflammation irrespective of disease duration. Brain 133(Pt 6):1591–1601
38. Prusky GT, Alam NM, Beekman S, Douglas RM (2004) Rapid quantification of adult and developing mouse spatial vision using a virtual optomotor system. Invest Ophthalmol Vis Sci 45(12):4611–4616
39. Porciatti V (2015) Electrophysiological assessment of retinal ganglion cell function. Exp Eye Res 141:164–170
40. Werneburg S, Jung J, Kunjamma RB, Ha SK, Luciano NJ, Willis CM et al (2020) Targeted Complement Inhibition at Synapses Prevents Microglial Synaptic Engulfment and Synapse Loss in Demyelinating Disease. Immunity 52(1):167–182 e7

41. Mey GM, Evonuk KS, Shelestak J, Irfan M, Wolfe LM, Laye SE et al (2024) Inhibiting AMPA receptor signaling in oligodendrocytes rescues synapse loss in a model of autoimmune demyelination. iScience 27(11):111226
42. Miura G, Wang MH, Ivers KM, Frishman LJ (2009) Retinal pathway origins of the pattern ERG of the mouse. Exp Eye Res 89(1):49–62
43. Quinn TA, Dutt M, Shindler KS (2011) Optic neuritis and retinal ganglion cell loss in a chronic murine model of multiple sclerosis. Front Neurol 2:50
44. Mey GM, Evonuk KS, Chappell MK, Wolfe LM, Singh R, Batoki JC et al (2022) Visual imaging as a predictor of neurodegeneration in experimental autoimmune demyelination and multiple sclerosis. Acta Neuropathol Commun 10(1):87
45. Jin J, Smith MD, Kersbergen CJ, Kam TI, Viswanathan M, Martin K et al (2019) Glial pathology and retinal neurotoxicity in the anterior visual pathway in experimental autoimmune encephalomyelitis. Acta Neuropathol Commun 7(1):125
46. Smith J, Bartel DP (2026) The G3BP stress-granule proteins reinforce the integrated stress response translation programme. Nat Cell Biol 28(1):135–148
47. Klein P, Kallenberger SM, Roth H, Roth K, Ly-Hartig TBN, Magg V et al (2022) Temporal control of the integrated stress response by a stochastic molecular switch. Sci Adv 8(12):eabk2022
48. Hecker C, Dietrich M, Issberner A, Hartung HP, Albrecht P (2020) Comparison of different optomotor response readouts for visual testing in experimental autoimmune encephalomyelitis-optic neuritis. J Neuroinflammation 17(1):216
49. Giolli RA, Blanks RH, Lui F (2006) The accessory optic system: basic organization with an update on connectivity, neurochemistry, and function. Prog Brain Res 151:407–440
50. Costa-Mattioli M, Walter P (2020) The integrated stress response: From mechanism to disease. Science 368(6489):eaat5314
51. Protter DSW, Parker R (2016) Principles and Properties of Stress Granules. Trends Cell Biol 26(9):668–679
52. Huang H, Miao L, Liang F, Liu X, Xu L, Teng X et al (2017) Neuroprotection by eIF2α-CHOP inhibition and XBP-1 activation in EAE/optic neuritiss. Cell Death Dis 8(7):e2936–e

Figures

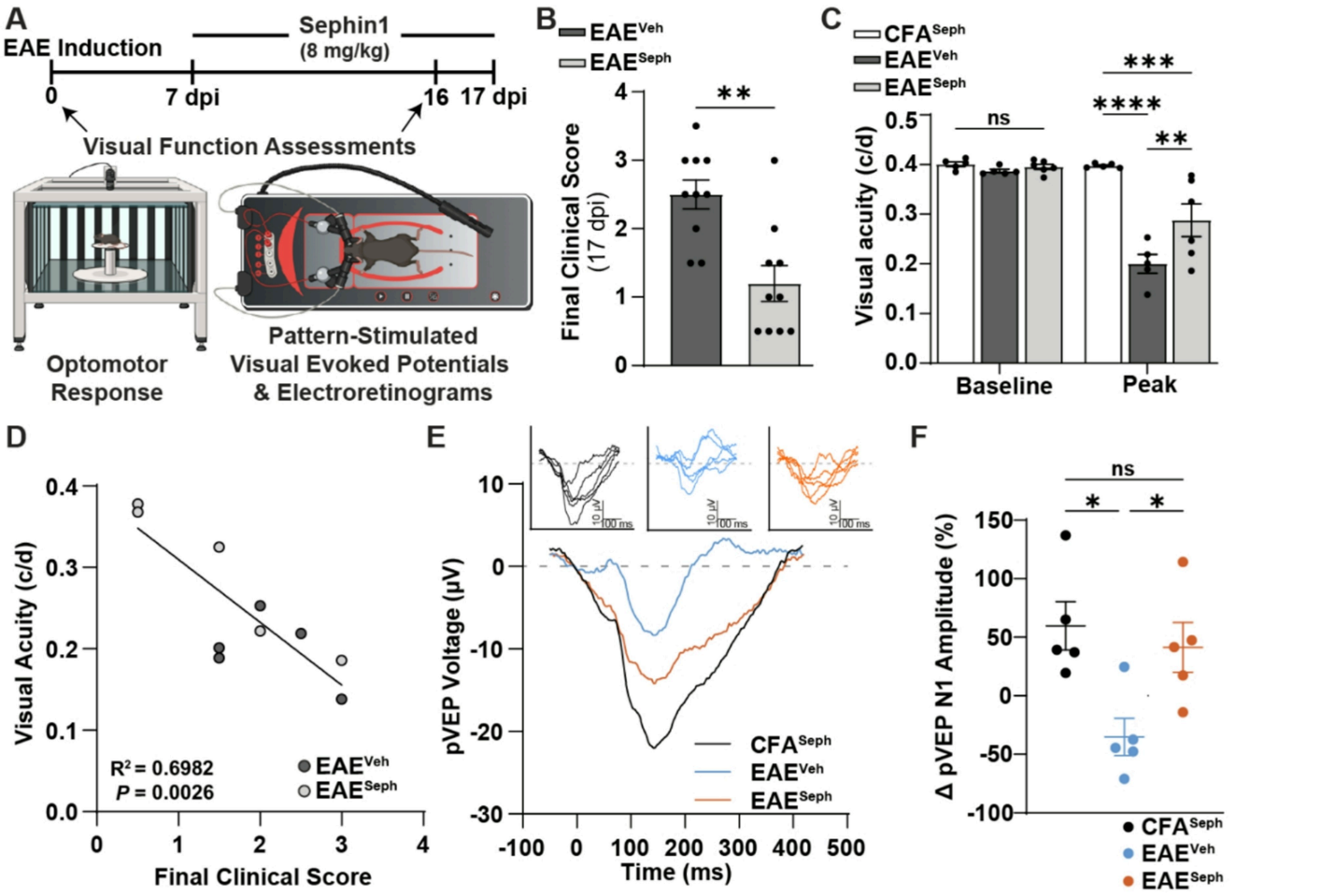


Figure 1

Prophylactic Sephin1 reduces EAE severity and preserves visual function at peak EAE. (A) Schematic of the experimental timeline: Baseline optomotor tests and pattern-stimulated visual evoked potentials (pVEP) and electroretinograms were performed at baseline (prior to EAE induction) and 16 days post-induction (dpi, arrows). Sephin1 (8 mg/kg) was administered intraperitoneally from 7-17 dpi, and tissue was harvested for analysis at 17 dpi (peak EAE). **(B)** Quantification of final EAE clinical scores shows a decrease in Sephin1-treated animals (EAE^{Seph}) compared to vehicle-treated (EAE^{Veh}) at 17 dpi. **(C)** Quantification of the optomotor response represented as visual acuity and measured in cycles/degree (c/d) shows that both EAE groups have significantly reduced vision compared to Sephin1-treated CFA controls (CFA^{Seph}), but that EAE^{Seph} mice have significantly preserved visual acuity compared to EAE^{Veh} mice. **(D)** Correlation of visual acuity with the final EAE clinical score shows a significant negative relationship between EAE clinical severity and visual acuity, regardless of experimental group. **(E)** Average pVEP traces across experimental groups. Insets show individual traces for each animal per group. **(F)** Quantification of the change in pVEP amplitude at 17 dpi relative to baseline shows a significant decrease in EAE^{Veh} compared to CFA^{Seph} controls, which is significantly preserved in EAE^{Seph}

mice. Data=mean±SEM, n=5/group. Statistical analyses: (B) Unpaired t test, *P*=0.0011, (C) two-way ANOVA with Tukey's post-hoc test, baseline: ns=not significant, *P*=0.8284 (CFA^{Seph} vs EAE^{Seph}); peak: CFA^{Seph} vs EAE^{Veh} *P*<0.0001; CFA^{Seph} vs EAE^{Seph} *P*=0.0001; EAE^{Veh} vs EAE^{Seph} *P*=0.0003, (D) simple linear regression, R^2=0.6982, *P*=0.0018, (F) one-way ANOVA with Tukey's post-hoc test, CFA^{Seph} vs EAE^{Veh} *P*=0.0123; CFA^{Seph} vs EAE^{Seph} *P*=0.7869; EAE^{Veh} vs EAE^{Seph} *P*=0.0407.

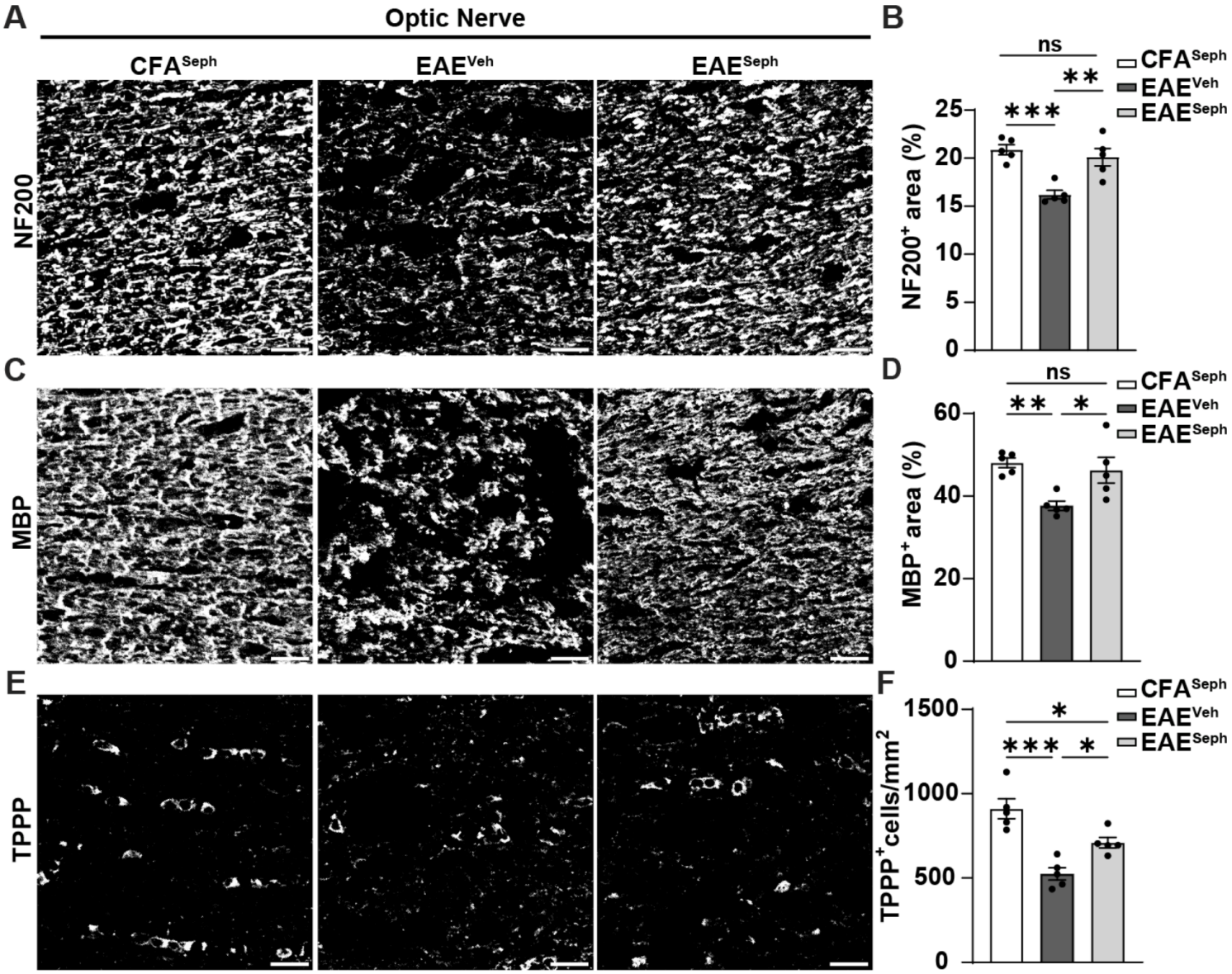


Figure 2

Sephin1 protects axons, myelin, and oligodendrocytes in the optic nerve at peak EAE. (A) Representative immunostaining against $NF200^+$ axons. **(B)** $NF200^+$ percent area was reduced in EAE^{Veh} mice compared with CFA^{Seph} controls and was preserved in EAE^{Seph} mice. **(C)** Representative immunostaining against MBP^+ myelin. **(D)** MBP^+ percent area was reduced in EAE^{Veh} mice compared with CFA^{Seph} controls and was preserved in EAE^{Seph} mice. **(E)** Representative immunostaining against $TPPP^+$ oligodendrocytes. **(F)** Quantification of $TPPP^+$ cells shows a significant decrease in both EAE^{Veh}

and EAE^{Seph} mice compared to CFA^{Seph} controls, with a significant preservation of cells in EAE^{Seph} compared to EAE^{Veh} mice. All scale bars=20µm. Data=mean±SEM, n=5/group. Statistical analyses: one-way ANOVA with Tukey's post-hoc test (B, D, F). ns=not significant, (B) CFA^{Seph} vs EAE^{Veh} *P*=0.0008; CFA vs EAE^{Seph} *P*=0.6894; EAE^{Veh} vs EAE^{Seph} *P*=0.0033, (D) CFA^{Seph} vs EAE^{Veh} *P*=0.0091; CFA vs EAE^{Seph} *P*=0.8066; EAE^{Veh} vs EAE^{Seph} *P*=0.0282, (F) CFA^{Seph} vs EAE^{Veh} *P*=0.0001; CFA vs EAE^{Seph} *P*=0.0182; EAE^{Veh} vs EAE^{Seph} *P*=0.0291.

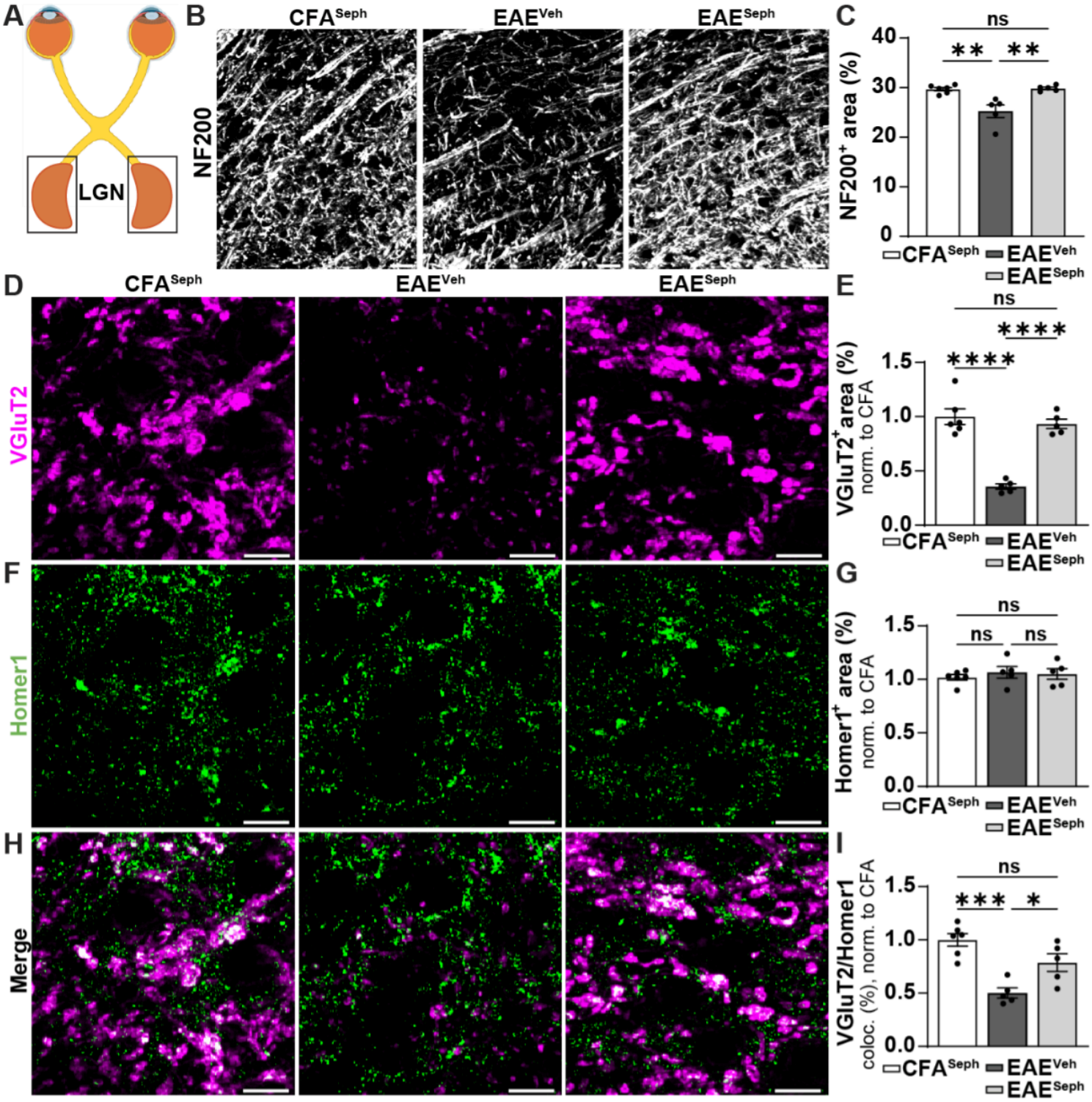


Figure 3

Sephin1 protects retinogeniculate axons and RGC presynaptic terminals at peak EAE. (A) Schematic of the anterior visual pathway with boxes around the region of interest, the lateral geniculate nucleus (LGN). **(B)** Representative immunostaining against $NF200^{+}$ axons. **(C)** Quantification of $NF200^{+}$ percent area shows a significant decrease in EAE^{Veh} mice that is significantly preserved in EAE^{Seph} compared to CFA^{Seph} controls. **(D)** Representative immunostaining against $VGluT2^{+}$ presynaptic terminals. **(E)** Quantification of $VGluT2^{+}$ percent area shows a significant decrease in EAE^{Veh} mice that is significantly preserved in EAE^{Seph} mice compared to CFA^{Seph} controls. **(F)** Representative immunostaining against $Homer1^{+}$ postsynaptic terminals. **(G)** Quantification of $Homer1^{+}$ percent area shows no statistical difference across experimental groups. **(H)** Representative images of colocalized VGluT2 and Homer1 signal. **(I)** Quantification of the colocalized VGluT2 and Homer1 percent area shows a significant decrease in EAE^{Veh} mice that is significantly preserved in EAE^{Seph} mice compared to CFA^{Seph} controls. Scale bars=20μm (B) and 10μm (D,F,H). Data=mean±SEM, n=5/group. Statistical analyses: one-way ANOVA with Tukey's post-hoc test (C, E, G, I). ns=not significant, (C) CFA^{Seph} vs EAE^{Veh} P=0.0020; CFA vs EAE^{Seph} P=0.9821; EAE^{Veh} vs EAE^{Seph} P=0.0020, (E) CFA^{Seph} vs EAE^{Veh} P<0.0001; CFA vs EAE^{Seph} P=0.6574; EAE^{Veh} vs EAE^{Seph} P<0.0001, (G) CFA^{Seph} vs EAE^{Veh} P=0.7180; CFA vs EAE^{Seph} P=0.8683; EAE^{Veh} vs EAE^{Seph} P=0.9622. (I) CFA^{Seph} vs EAE^{Veh} P=0.0003; CFA vs EAE^{Seph} P=0.0840; EAE^{Veh} vs EAE^{Seph} P=0.0249.

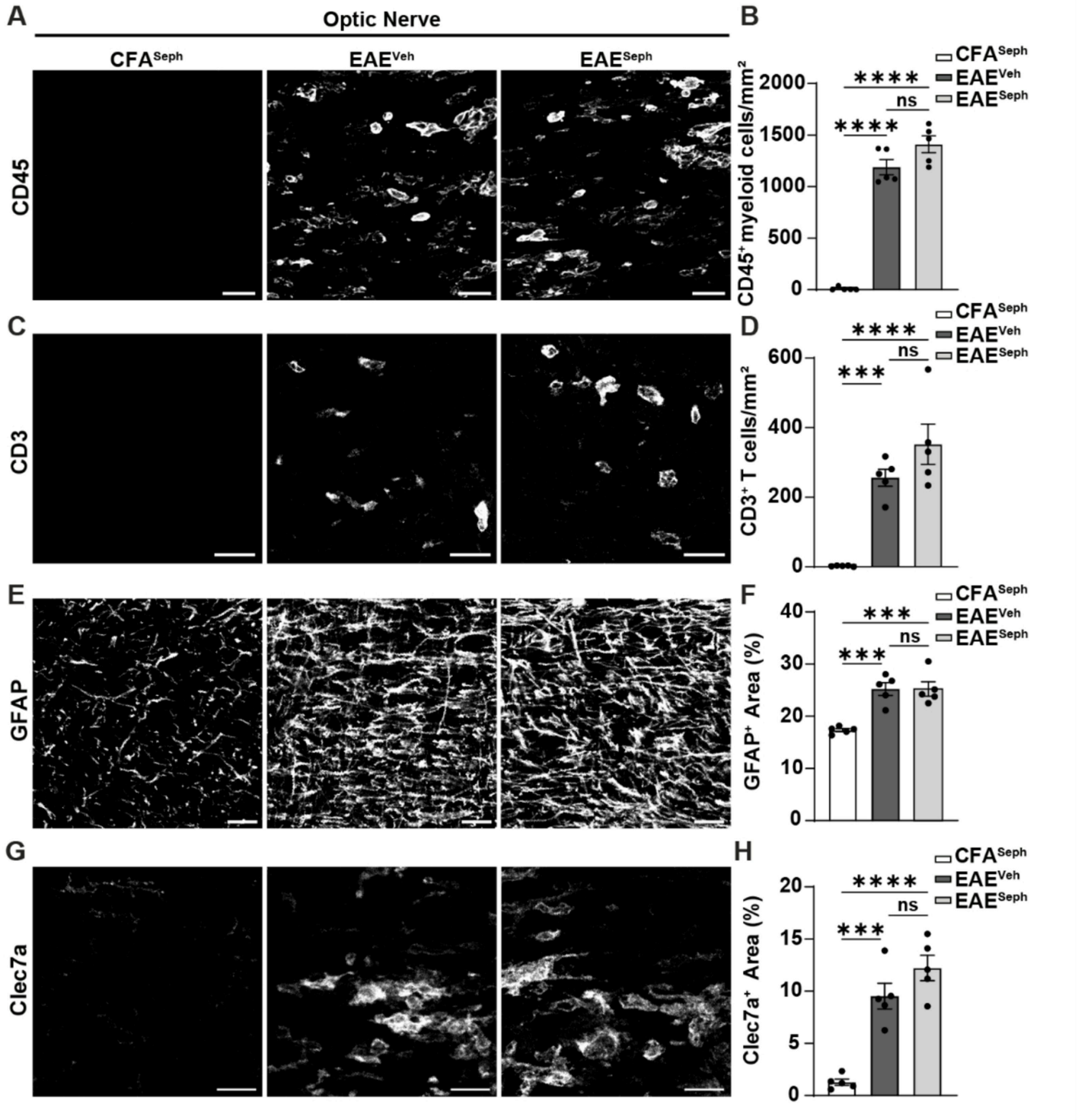


Figure 4

Sephin1 does not reduce optic nerve inflammation at peak EAE. (A) Representative immunostaining against $CD45^+$ immune cells. **(B)** Quantification of $CD45^+$ myeloid cells per square millimeter shows a significant increase in both EAE groups compared to CFA^{Seph} controls, with no significant differences between EAE^{Veh} and EAE^{Seph} mice. **(C)** Representative immunostaining against $CD3^+$ T cells. **(D)** Quantification of $CD3^+$ T cells per square millimeter shows a significant increase in both EAE^{Veh} and

EAE^{Seph} mice compared to CFA^{Seph} controls, with no significant differences between the EAE groups. **(E)** Representative immunostaining against $GFAP^+$ astrocytes. **(F)** Quantification of $GFAP^+$ percent area shows a significant increase in both EAE groups compared to CFA^{Seph} controls, with no significant differences between EAE^{Veh} EAE^{Seph} mice. **(G)** Representative immunostaining against $Clec7a^+$ microglia. **(H)** Quantification of $Clec7a^+$ percent area shows a significant increase in both EAE groups compared to CFA^{Seph} controls, with no significant differences between EAE^{Veh} EAE^{Seph} mice. All scale bars=20μm (A,C,E,G). Data=mean±SEM, n=5/group. Statistical analyses: one-way ANOVA with Tukey's post-hoc test (B, D, F, H). ns=not significant, (B) CFA^{Seph} vs EAE^{Veh} $P<0.0001$; CFA^{Seph} vs EAE^{Seph} $P<0.0001$; EAE^{Veh} vs EAE^{Seph} $P=0.0719$, (D) CFA^{Seph} vs EAE^{Veh} $P=0.0009$; CFA^{Seph} vs EAE^{Seph} $P<0.0001$; EAE^{Veh} vs EAE^{Seph} $P=0.1900$, (F) CFA^{Seph} vs EAE^{Veh} $P=0.0006$; CFA^{Seph} vs EAE^{Seph} $P=0.0006$; EAE^{Veh} vs EAE^{Seph} $P>0.9999$. (H) CFA^{Seph} vs EAE^{Veh} $P=0.0005$; CFA^{Seph} vs EAE^{Seph} $P<0.0001$; EAE^{Veh} vs EAE^{Seph} $P=0.2750$.

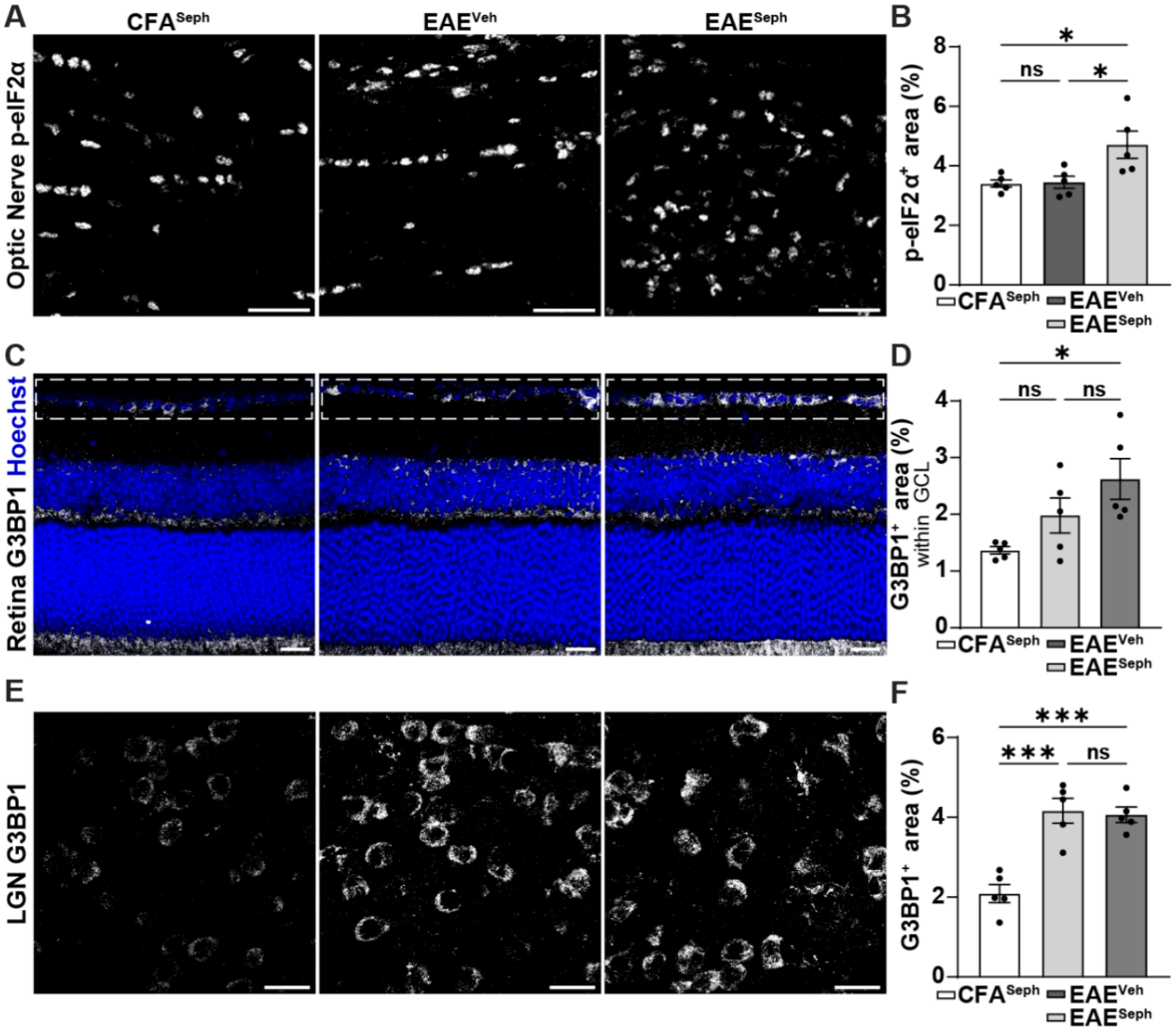


Figure 5

p-eIF2α expression is preferentially increased in the optic nerve in Sephin1-treated EAE animals. (A) Representative immunostaining against phosphorylated eIF2α (p-eIF2α). **(B)** Quantification of p-eIF2α^{+} percent area in the optic nerve shows a significant increase in EAE^{Seph} mice compared to CFA^{Seph} controls and EAE^{Veh} mice. **(C)** Representative immunostaining against G3BP1^{+} stress granules in the ganglion cell layer (GCL) of the retina. **(D)** Quantification of G3BP1^{+} percent area in the GCL shows a significant increase in EAE^{Seph} mice compared to CFA^{Seph} controls, with no significant change relative to EAE^{Veh} mice. **(E)** Representative immunostaining against G3BP1^{+} stress granules in the LGN. **(F)** Quantification of G3BP1^{+} percent area in the LGN shows a significant increase in EAE groups compared to CFA^{Seph} controls, with no significant change between EAE^{Veh} and EAE^{Seph} mice. All scale bars=20μm.

Data=mean±SEM, n=5/group. Statistical analyses: one-way ANOVA with Tukey's post-hoc test (B, D, F). ns=not significant, (B) CFA^{Seph} vs EAE^{Veh} P=0.9944; CFA^{Seph} vs EAE^{Seph} P=0.0245; EAE^{Veh} vs EAE^{Seph} P=0.0294, (D) CFA^{Seph} vs EAE^{Veh} P=0.2918; CFA^{Seph} vs EAE^{Seph} P=0.0184; EAE^{Veh} vs EAE^{Seph} P=0.2641, (F) CFA^{Seph} vs EAE^{Veh} P=0.0002; CFA^{Seph} vs EAE^{Seph} P=0.0003; EAE^{Veh} vs EAE^{Seph} P=0.9567.

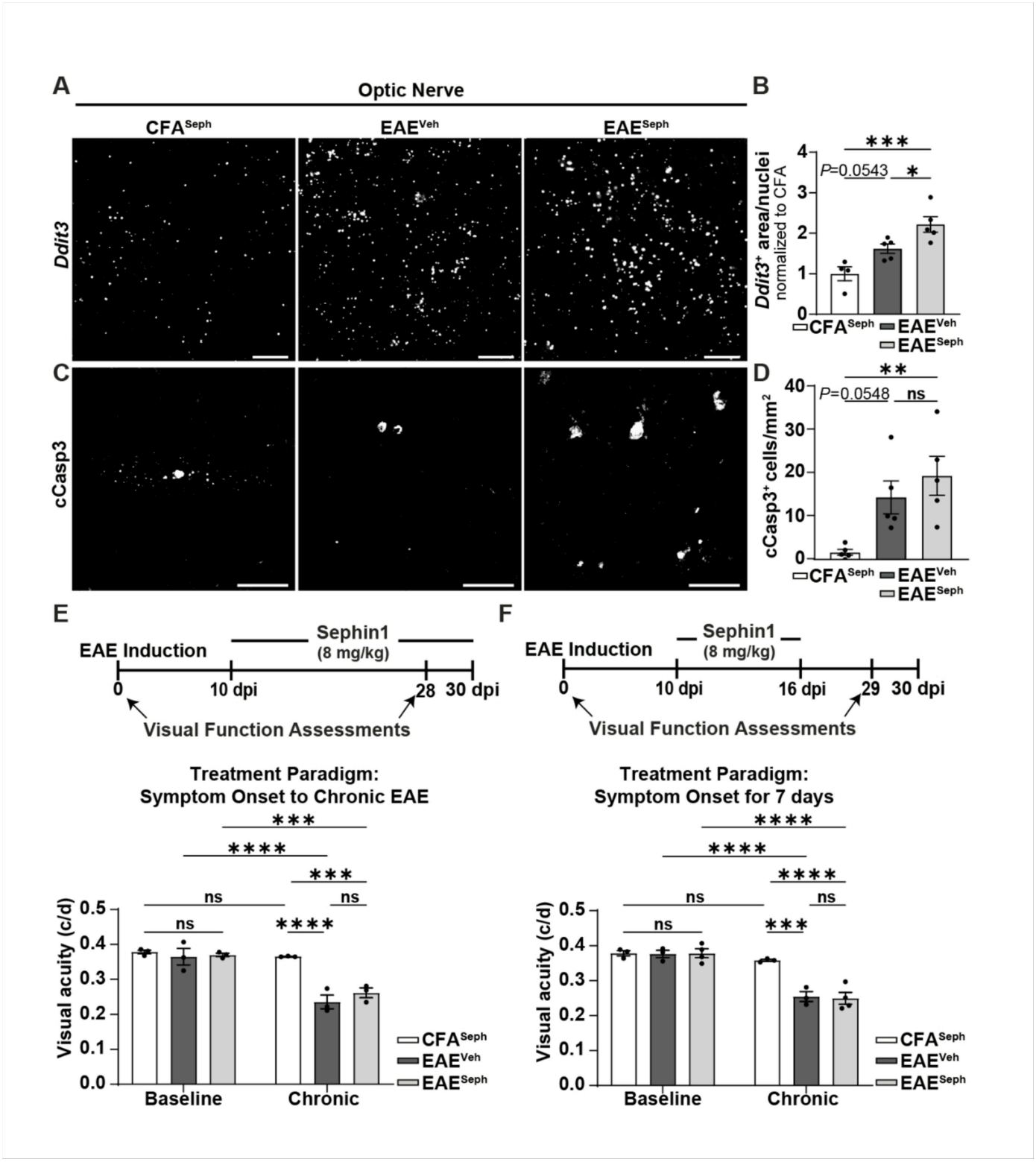


Figure 6

Sephin1-induced optic nerve *Ddit3* enrichment accompanies failed chronic visual protection. (A-D) Prophylactic treatment paradigm: **(A)** Representative immunostaining against *Ddit3*, which encodes CHOP. **(B)** Quantification of *Ddit3*$^{+}$ percent area, per total number of Hoechst^{+} nuclei, in the optic nerve shows a significant increase in EAE^{Seph} mice compared to CFA^{Seph} controls and EAE^{Veh} mice. **(C)** Representative immunostaining against the cleaved caspase-3 (cCasp3)$^{+}$ marker of apoptosis. **(D)** Quantification of cCasp3^{+} cells shows a significant increase in EAE^{Seph} mice compared to CFA^{Seph} controls, with no significant change relative to EAE^{Veh} mice. **(E)** Quantification of visual acuity at baseline and chronic EAE (28 dpi) when Sephin1 treatment began after EAE symptom onset until chronic EAE. Results indicate that both EAE^{Veh} and EAE^{Seph} mice have reduced visual acuity at chronic EAE compared to CFA^{Seph} controls, with no significant change between EAE groups. **(F)** Quantification of visual acuity at baseline and chronic EAE (29 dpi) when Sephin1 treatment began after EAE symptom onset and continued only for 7 days. Results indicate that both EAE^{Veh} and EAE^{Seph} mice have reduced visual acuity at chronic EAE compared to CFA^{Seph} controls, with no significant change between EAE groups. All scale bars=20μm. Data=mean±SEM, n=3-5/group. Statistical analyses: one-way ANOVA with Tukey's post-hoc test (B,D), two-way ANOVA with Tukey's post-hoc test (E-F). ns=not significant, (B) CFA^{Seph} vs EAE^{Veh} P=0.0543; CFA^{Seph} vs EAE^{Seph} P=0.0008; EAE^{Veh} vs EAE^{Seph} P=0.0484, (D) CFA^{Seph} vs EAE^{Veh} P=0.0548; CFA^{Seph} vs EAE^{Seph} P=0.0088; EAE^{Veh} vs EAE^{Seph} P=0.5753, (E) Baseline: CFA^{Seph} vs EAE^{Veh} P=0.7839; CFA^{Seph} vs EAE^{Seph} P=0.9081; EAE^{Veh} vs EAE^{Seph} P=0.9657; Chronic: CFA^{Seph} vs EAE^{Veh} P<0.0001; CFA^{Seph} vs EAE^{Seph} P=0.0006; EAE^{Veh} vs EAE^{Seph} P=0.4167; Baseline-to-Chronic: CFA P=0.5354, EAE^{Veh} P<0.0001, EAE^{Seph} P=0.0001. (F) Baseline: CFA^{Seph} vs EAE^{Veh} P=0.9918; CFA^{Seph} vs EAE^{Seph} P=0.9997; EAE^{Veh} vs EAE^{Seph} P=0.9937; Chronic: CFA^{Seph} vs EAE^{Veh} P=0.0003; CFA^{Seph} vs EAE^{Seph} P<0.0001; EAE^{Veh} vs EAE^{Seph} P=0.9607; Baseline-to-Chronic: CFA P=0.2985, EAE^{Veh} P<0.0001, EAE^{Seph} P<0.0001.

Supplementary Files

This is a list of supplementary files associated with this preprint. Click to download.

- 260630SupplementalFiguresFinal.pdf